Supersonic Retropropulsion Technology for Application to High Mass Mars Entry, Descent, and Landing

Space Systems Design Laboratory (SSDL)
Guggenheim School of Aerospace Engineering
Georgia Institute of Technology
Atlanta, GA

Author:
Ashley M. Korzun

Advisor:
Dr. Robert D. Braun

April 30, 2008

Supersonic Retropropulsion Technology for Application to High Mass Mars Entry, Descent, and Landing

Ashley M. Korzun
Georgia Institute of Technology, Atlanta, GA 30332

Dr. Robert D. Braun
Faculty Advisor, Georgia Institute of Technology, Atlanta, GA 30332

As vehicle masses continue to increase for missions involving atmospheric entry, supersonic deceleration is challenging the qualifications and capabilities of Viking-heritage entry, descent, and landing (EDL) technology. At Mars, high entry masses and insufficient atmospheric density often result in unacceptable parachute deployment and operating conditions, requiring the exploration of alternative approaches to supersonic deceleration. Supersonic retropropulsion, the initiation of a retropropulsion phase while the vehicle is still traveling supersonically, may be an enabling technology for systems with high ballistic coefficients operating in thin atmospheres such as at Mars. The relevance of this technology to the feasibility of Mars EDL has been shown to increase with ballistic coefficient to the point that it is likely required for human Mars exploration. In conjunction with a literature review of supersonic retropropulsion technology as it applies to blunt body entry vehicles, a systems study was performed to assess the impact of supersonic retropropulsion on high mass Mars EDL. This investigation addresses the applicability, limitations, and performance implications of supersonic retropropulsion technology in the context of future human and robotic Mars exploration missions.

Nomenclature

T/W	=	thrust-to-weight
T	=	thrust, N
P_0	=	total pressure, N/m^2
A^*	=	nozzle throat area, m^2
C_T	=	thrust coefficient
q_∞	=	freestream dynamic pressure, N/m^2
A	=	reference area, m^2
β	=	ballistic coefficient, kg/m^2
m_{prop}	=	propellant mass, kg
M_∞	=	freestream Mach number
C_D	=	atmospheric drag coefficient
$C_{A,total}$	=	total axial force coefficient
C_M	=	pitching moment coefficient
α	=	angle of attack
υ	=	flow direction at nozzle exit
γ_∞	=	freestream specific heat ratio
P_e	=	static pressure at nozzle exit, N/m^2
P_∞	=	freestream static pressure, N/m^2
ρ_∞	=	freestream density, kg/m^3
V_∞	=	freestream velocity, m/s
γ_e	=	specific heat ratio of nozzle exhaust
M_e	=	Mach number at nozzle exit
A_e	=	area of nozzle exit, m^2
I_{sp}	=	specific impulse, s
r	=	distance from planet center, m
V	=	velocity with respect to planet, m/s
γ	=	flight path angle
θ	=	longitude
ψ	=	heading angle
ϕ	=	latitude
ω	=	angular rotation rate of planet, rad/s
σ	=	bank angle
g	=	local gravitational accel., m/s^2
g_E	=	Earth gravitational accel., m/s^2
ε	=	angle between thrust and velocity
m	=	vehicle mass, kg
L	=	lift, N
D	=	drag, N
h	=	altitude above the planet surface, m

I. Introduction

In most current EDL systems, decelerating the vehicle from hypersonic to subsonic speeds is achieved using the aerodynamic drag of the entry vehicle and other aerodynamic decelerators such as parachutes[1]. At Mars, high entry masses and insufficient atmospheric density often result in unacceptable parachute deployment and operating conditions. An alternative deceleration approach is to initiate retropropulsion while the vehicle is still traveling supersonically. Supersonic retropropulsion may be an enabling technology for systems with high ballistic coefficients operating in thin atmospheres such as at Mars.

Investigation into the interaction of supersonic retropropulsion with blunt body aerodynamics began in the early 1950s. Experimental work with small-scale wind tunnel models by Love[2,3,4], Huff and Abdalla[5], and Moeckel[6,7] focused on shock-boundary layer phenomena and the effects of nozzle flow on boundary layer transition. These investigations were among the earliest observations of the aerodynamic drag reductions and associated flowfield stability transitions for configurations with a nozzle located along the body centerline. Moeckel[6,7] was among the first to observe an aerodynamic drag reduction in supersonic retropropulsion configurations with a centerline nozzle application. Moeckel[6,7] also observed flow separation on the forebody with the same configuration. Both effects were later observed in other experiments with a supersonic retropropulsion nozzle along the centerline of a blunt entry body[15,18-21,23-28,34-35,37,39-41].

These early works are consistent in observing that increasing thrust coefficient (defined in Eq. 1) moves the boundary layer transition closer to the nose of the body[2]. Additional work[4,5,8,9] on supersonic jet flow and jet-body interactions laid the groundwork for future wind tunnel testing of supersonic nozzle exhaust effects on body surface pressure distributions and flowfield stability. While many of these body shapes were not the blunted-cone entry vehicle shapes flown in the 1960s and 1970s, these works established the fundamental physics of shock-boundary layer interactions and motivated later investigations to apply such interaction effects to blunt body entry vehicles for planetary exploration.

This early retropropulsion work was extended to blunt body entry geometries in the 1960s and early 1970s, primarily through wind tunnel experiments on small-scale models. Among the concepts investigated were single and multiple nozzle configurations, with the retropropulsion nozzles placed at either the center or the periphery of the vehicle forebody. Experimental results for low thrust coefficients consistently show significant increases in the total axial force coefficient (summation of aerodynamic drag and thrust) for peripheral nozzle locations[15,25-26]. In contrast, aerodynamic drag reduction was observed for centerline nozzle locations[15,18-21,23-25,27-28,34-35,37,39-41]. For high thrust coefficients, all nozzle configurations contributed substantially to the effective total axial force on the vehicle, though by thrust contributions only (no aerodynamic drag contribution)[15,18,20-21,23-24,26-27]. Additionally, the stability of the flowfield and resulting aerodynamic effects were found to be strongly dependent on the ratio of total pressure between the retropropulsion and the freestream[15,18-21,23-28,34-35,37,39-41].

Although the majority of the literature is focused on deceleration applications, the aerothermal effects of supersonic retropropulsion, the development of test scaling parameters, and the capabilities of computational analysis have also been explored[15,19,21,34-45]. Both experimental and computational work show the aerothermal effects of retropropulsion to be important, with the potential for heat transfer to the body to be doubled when combustion products are injected into the shock layer.

Experimental work has produced relationships for scaling and developed the primary similarity parameters for model and nozzle design. Computational investigation has recently been renewed and early code validation efforts show good agreement with experimental data for axisymmetric configurations. While computational solutions are in agreement with experimental data for stable flowfield conditions, these computational models may be unable to accurately capture the complete physical behavior for unstable flowfield conditions.

This paper provides a survey of the literature on the effects of retropropulsion on blunt body entry vehicles in an opposing supersonic or hypersonic freestream. The focus is on aerodynamic performance effects for application to EDL design and computational simulation development. This paper does not discuss non-propulsive supersonic decelerators, reaction control system interactions, detailed aerothermodynamic issues, slender-body geometries, or exhaust plumes in directions other than against the freestream. Section 2 discusses past Mars EDL systems studies and the retropropulsion sizing models used in those analyses. Sections 3 and 4 compare results in the literature for central and peripheral nozzle locations, as well as the effects of variations in environment and design parameters such as nozzle geometry and chemical composition of the freestream and retrorocket exhaust, providing a summary of the existing experimental database. Section 5 discusses the computational simulation of supersonic retropropulsion flowfields and the extensibility and limitations of this work. Section 6 summarizes the literature review. Section 7 characterizes the performance of supersonic retropropulsion technology in terms of propellant

mass fraction as vehicle ballistic coefficient increases across a range of initiation conditions consistent with future robotic and human Mars exploration missions.

II. Past Retropropulsion Systems Studies

To date, the United States has successfully landed five robotic missions on Mars: Viking 1, Viking 2, Mars Pathfinder, and the two Mars Exploration Rovers. Including missions launched by the end of the decade, the largest payload mass landed on Mars will be Mars Science Laboratory (MSL), whose rover is approaching 900 kg. The EDL systems for these missions rely heavily on extensions of Viking-heritage technology, namely supersonic Disk-Gap-Band (DGB) parachutes, 70º sphere-cone blunt body aeroshells, and subsonic propulsive terminal descent[1].

The focused technology development program preceding the Viking missions in the 1960s and 1970s developed supersonic retropropulsion to nearly the level of maturity the concept has today. The eventual selection of a supersonic DGB parachute system and subsonic propulsive terminal descent phase for the Viking landers ended much of the research efforts to develop supersonic retropropulsion. Only recently has interest in supersonic retropropulsion resurfaced. The applicability of Viking EDL technologies to the high mass planetary entries needed for human Mars exploration has been shown to be constrained by deployment conditions and performance at higher Mach numbers of supersonic DGB parachutes[1]. This resurgence of interest in human Mars exploration has resulted in systems-level studies to assess the required performance of these high-mass entry systems, and the conclusions of these studies, in general, recommend the development of alternative supersonic decelerators, a challenge potentially addressed by supersonic retropropulsion.

Human Mars architecture studies[10,11,12,13] predict payload masses on the order of 20 to 100 t. The EDL requirements of these high mass, high ballistic coefficient systems extend well beyond the capabilities of many Viking-heritage EDL technologies. Supersonic deceleration is possibly the most critical deficiency in extending these heritage technologies. The high ballistic coefficients in these architecture studies ($\sim$300 kg/m^2 and higher), thin Mars atmosphere, and inability to extend supersonic DGB parachutes to the required dimensions and deployment conditions severely reduce the timeline available for deceleration and the transition from a hypersonic entry vehicle to a terminal landing configuration.

The point design in NASA's 1998 Mars Design Reference Mission[10,11] attempts to address the supersonic deceleration gap by using clusters of 50 m diameter supersonic parachutes, followed by a subsonic propulsive terminal descent. Alternatively, Christian, et al.[12] replaced the traditional parachute system with a purely propulsive descent, initiated at supersonic velocities. Because these studies are for human class missions, with payload masses ranging from 20 to 100 t, significantly larger propulsion systems are required than have been flown previously. In these studies, the descent propulsion systems for supersonic deceleration have been assumed to be LOX/methane RD-180 derivatives, with an engine thrust to weight (T/W) of 80 and maximum thrust of 1 MN[12,14]. A thrust magnitude of 1 MN for an RD-180 derivative engine corresponds to a thrust coefficient of approximately 0.9. The thrust coefficient is defined as the ratio of the thrust, T, to the nozzle operating pressure, p_0, and throat area, A^*:

$$C_T = \frac{T}{P_0 A^*} = \frac{T}{q_\infty A} \tag{1}$$

Past literature demonstrates that, for a retropropulsion configuration where the nozzles are located on the forebody periphery, the maximum increase in total axial force coefficient (aerodynamic drag and thrust contributions) occurs near conditions corresponding to a thrust coefficient of 1.0[15]. Hence, proper modeling of the supersonic retropropulsion system can have a dramatic impact on EDL architectural performance. These aerodynamic effects are discussed in Section 4.

Prior robotic Mars missions have had vehicle T/W values on the order of 3[1]. For three future mission payload cases (20, 40, and 70 t)[11] and a fixed maximum thrust magnitude of 1.0 MN, the required vehicle T/W and thrust coefficient will be different from past robotic missions (i.e., $T/W \approx$ 2.3 or 1.5 vs. 3.0). The trajectories from Christian, et al.[12] limited the maximum deceleration to 5 g's during descent, requiring a variable thrust level to slow the vehicle to subsonic velocities. Table 1a gives the required vehicle T/W and thrust coefficient for a fixed maximum thrust (T_{max}) for payload masses of 20, 40, and 70 t. Table 1b gives the required maximum thrust and thrust coefficient for a fixed vehicle T/W of 3.0 for these three payload masses.

Table 1. *T/W* Comparison for Human Mars Missions

a.)

| Payload Mass (t) | Entry Mass (t) | Fixed Max Thrust | | |
		T_{max}	T/W	C_T
20	79	1.0 MN	3.40	0.87
40	115	1.0 MN	2.33	0.87
70	176	1.0 MN	1.52	0.87

b.)

| Payload | Entry | Fixed T/W | | |
		T/W	T_{max}	C_T
20	79	3.0	0.88 MN	0.87
40	115	3.0	1.29 MN	0.87
70	176	3.0	1.97 MN	0.87

Of the past Mars EDL architectural studies, only the investigations by Christian, and Wells, et al.[12,13] initiate retropropulsion at supersonic conditions. In these two references, the aerodynamic interaction of supersonic retropropulsion was not modeled (i.e., the deceleration was assumed to be independent of nozzle location). In addition, the aerodynamic drag was set to zero, and only the axial force due to thrust was modeled. Past experimental evidence suggests that, for configurations with the nozzles located at the forebody periphery, inclusion of aerodynamic interaction effects into supersonic retropropulsion performance models will reduce the propellant mass required.

The general relationship between the required descent propellant mass fraction and vehicle ballistic coefficient is shown in Figure 1. Descent propellant mass fraction is defined as the ratio of propellant mass required to decelerate the vehicle from supersonic retropropulsion initiation to subsonic conditions to entry mass. This figure illustrates the increasing impact of aerodynamic effects on required descent propellant mass fraction as ballistic coefficient increases for a 15 m diameter Apollo aeroshell and $C_T = 1.0$. The data presented is for the minimum Mach initiation to reach subsonic conditions at 3 km altitude. Table 2 provides a summary of Figure 1 in terms of supersonic descent propellant mass. A detailed systems analysis from which these results were extracted is presented in Section 7. However, the ability of retropropulsion to substantially alter the aerodynamic characteristics of an entry vehicle at supersonic velocities with a *T/W* consistent or even lower than required for past missions suggests the possibility of using retropropulsion to close the supersonic deceleration technology gap.
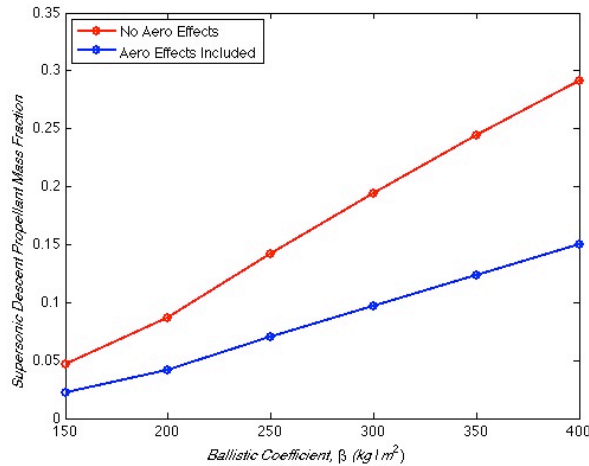

Figure 1. Descent Propellant Mass Fraction Impact of Neglecting Aerodynamic Effects During Supersonic Deceleration for a Configuration with Nozzles Located at the Vehicle Periphery for $C_T = 1.0$.

Table 2. Impact of Aerodynamic-Propulsive Interactions on Supersonic Descent Propellant Mass with Increasing Ballistic Coefficient

β (kg/m^2)	Entry Mass (kg)	m_{prop} (kg) – Aero Not Included	m_{prop} (kg) – Aero Included	Difference (kg)
150	34459	1616	772	**- 844**
200	45946	3951	1916	**- 1990**
250	57432	8144	4003	**- 4141**
300	68919	13549	6774	**- 6775**
350	80405	19659	9954	**- 9705**

As discussed in Section 4, a configuration with retronozzles located at the periphery of the forebody is most effective for supersonic deceleration, increasing the total axial force on the entry vehicle by approximately a factor of 2 for a thrust coefficient near 1.0[15]. As such, the positive impact of aerodynamic drag on reducing propellant mass fraction is reduced significantly for higher thrust coefficients or nozzle locations near the vehicle centerline. Experimentally observed aerodynamic and configuration trends for systems utilizing supersonic retropropulsion are discussed in detail in Sections 3 and 4.

III. General Flow Characteristics

Supersonic nozzle flow exhausting from a blunt body opposing a supersonic freestream results in an interaction between the nozzle flow and the detached bow shock. Resultant flowfields surrounding blunt bodies with no retropropulsion, configurations with nozzle flow from the center of the vehicle forebody, and configurations with nozzle flow from the periphery of the vehicle forebody each exhibit fundamentally different behavior. Flowfield geometry and stability are highly dependent on the nozzle location (central vs. peripheral) and the relative strength of the nozzle flow, often given as a function of the ratio of the total pressure of the jet flow to the total pressure of the freestream. For a fixed set of freestream conditions, characterized by freestream total pressure, thrust coefficient may be used as a similarity parameter to gauge the strength of the nozzle flow relative to the freestream. As a result, the thrust coefficient is used as an independent parameter in this analysis when the freestream conditions are fixed. To compare resultant effects at different freestream conditions, the total pressure ratio is used.

A. Blunt Bodies without Retropropulsion

As a blunt entry body travels through the atmosphere of a planet, the flowfield surrounding the vehicle evolves as it descends to the surface. By the time aerodynamic drag has decelerated the vehicle to supersonic speeds, the vehicle is deep within the continuum flow regime where the Navier-Stokes equations are valid[16]. In the continuum flow regime, the flow over a blunt entry vehicle is characterized by a strong detached bow shock[17].

The primary flow features are also strong functions of the sonic line location between the bow shock and the body. If the sonic line is over the nose of the vehicle, the pressure distribution downstream of the sonic line is flat from the nose to the shoulder[16]. Newtonian methods are adequate to predict the pressure distribution, and subsequently the static aerodynamic coefficients in this case. However, if the sonic line is nearer the shoulder of the vehicle, the pressure distribution is monotonically decreasing away from the nose, and Newtonian methods will over and under-predict the pressure distributions at the nose and shoulder, respectively[16]. When the sonic line remains close to the boundary layer over most of the vehicle, the pressure distributions near the shoulder of the vehicle can change rapidly. Coupled with the large moment arm, these changes in pressure distribution can cause a significant variation in the static aerodynamic moment coefficient[16].

For blunt bodies without retropropulsion, flow separation typically occurs near the shoulder, where the flow turning angle is large. The region of high pressure behind the vehicle creates recirculation regions composed of the separated flow. The extent of the separation decreases with decreasing Reynolds number[16].

B. Central Retropropulsion Configurations

The majority of the literature focuses on retropropulsion configurations where either a single nozzle or small cluster of nozzles is located along the body centerline on the forebody. An example of a central retropropulsion configuration with a single nozzle is shown in Figure 2.

Figure 2. Example of a Central Retropropulsion Configuration with a Single Nozzle

Figure 3 (adapted[18]) illustrates the characteristic flowfield features for a central configuration and the complexity of the interaction between the nozzle flow and the freestream shock structure. The primary flow structures are the bow shock, free stagnation point, jet terminal shock, and the recirculation regions[18]. The location, degree of

formation, and stability of these features are a strong function of the ratio of jet total pressure to freestream total pressure. This total pressure ratio is often represented by thrust coefficient, assuming a fixed freestream stagnation pressure for a given test condition[18].
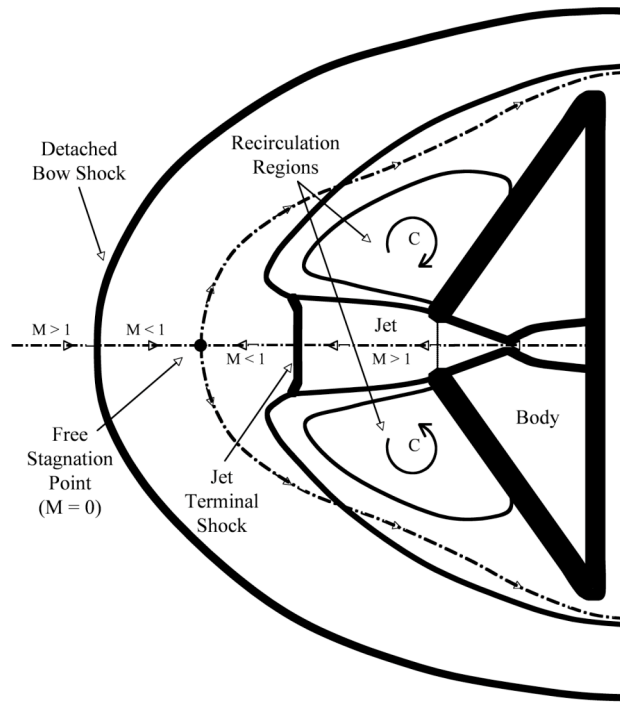

Figure 3. Characteristic Flowfield Features (adapted[18])

The entire flowfield structure is dependent on the formation of the stagnation point. The freestream must decelerate to zero velocity, first from supersonic to subsonic through a shock wave, then from subsonic to zero velocity at the stagnation point[18]. The nozzle flow undergoes a similar deceleration through mixing, viscous dissipation, or a normal shock, depending on the strength of the nozzle exhaust flow. For the case of supersonic retropropulsion, the stagnation region consists of two supersonic regions, the freestream and nozzle flow, and a subsonic region divided by a contact discontinuity, the stagnation point[19].

The interaction of the jet with the opposing supersonic freestream in central configurations has been observed to cause the flowfield to transition from stable to highly unstable and back to stable as the total pressure ratio (or thrust coefficient) increases[18,20]. This behavior is shown by Mach number contours in Figure 4[21]. A stable flowfield occurs when the bow shock is close to the body, and the jet flow does not penetrate the bow shock; in this case, the flowfield structure is not oscillating. An unstable flowfield occurs when the jet shock penetrates the bow shock and the total shock displacement is significantly greater than the displacement characteristic of the stable condition. This displacement increases to a maximum with increasing total pressure ratio and then collapses back to a displacement similar to the original stable case[15,19,21].
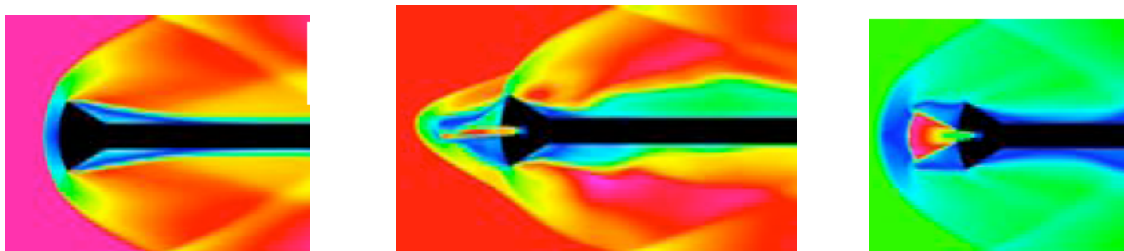

Figure 4. Stability Transitions With Increasing Jet Flow for Central Configurations (CFD Solutions[21])

This stability transition phenomenon is not thoroughly understood. However, the boundaries of the different flow regimes can be partially correlated to changes in relative mass flow and by increases in the ratio of jet total pressure to freestream total pressure. At low flow rates (low total pressure ratios), the exhaust flow is retained within the boundary layer and lacks sufficient momentum to disturb the bow shock[19].

As the nozzle flow rate increases, the nozzle flow cannot be contained within the boundary layer and begins to interact with the bow shock. The shock standoff distance increases proportionally with increasing nozzle flow until reaching a maximum displacement on the order of 6-7 body diameters[20]. In this unstable regime, the dissipative mechanism that allows the jet stagnation pressure to equal the freestream stagnation pressure at the interface is viscosity. These viscous losses require a greater jet length for the pressure adjustment to occur[20].

As the flow rate increases further, the shock standoff distance rapidly decreases, and the entire flow structure collapses back to a stable condition. In this case, the dissipative mechanism is a terminal shock, with the resulting subsonic jet flow stable enough to form a clear stagnation point[19,20]. The nozzle exit Mach number determines the expansion condition of the jet flow (underexpanded or overexpanded), hence determining which of the dissipative mechanisms is dominant. Mixing and viscous dissipation is typically associated with underexpanded jet flow, and shock dissipation is common of overexpanded jet flow[20,22]. This transition from a stable flowfield to an unstable flowfield occurs at lower thrust coefficients for smaller nozzles and at larger coefficients for larger nozzles, indicating dependence on the ratio of nozzle exit diameter to body diameter[23].

For multiple nozzles arranged about the body axis of symmetry close to the vehicle centerline, Peterson and McKenzie[24] observed the same stability transitions as seen for the single, centrally-located nozzle. At low flow rates, the nozzle flows do not interact with one another. However, as the flow rate increases, the individual jet flows begin to coalesce into a single jet flow and interact with the bow shock, resulting in large shock displacement.

C. Peripheral Retropropulsion Configurations

In contrast to the central retropropulsion configuration, few references are available on retropropulsion configurations with nozzles at the periphery of the forebody. The primary documented investigations on peripheral configurations are experimental work by Jarvinen and Adams[15,25] and Keyes and Hefner[26].

In a peripheral retropropulsion configuration, such as the one shown in Figure 5, the nozzle flow interacts with the bow shock differently than in a central configuration. The flow from each nozzle is swept away from the forebody and, at low flow rates, diffused into the opposing freestream by mixing[15]. Accordingly, flowfields for peripheral configurations do not have the large recirculation regions over the body surface characteristic of central configurations. Rather, the flowfield has a uniform region of high pressure inboard of the nozzles, resulting from the lack of disturbance to the portion of the bow shock nearest the nose of the blunt body. A smaller flow turning angle is required than for a central configuration, preventing the nozzle flow from disturbing the center of the bow shock.
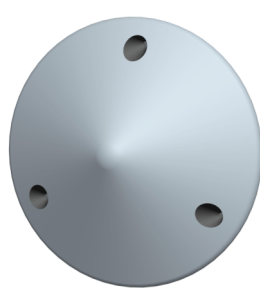

Figure 5. Example of a Peripheral Retropropulsion Configuration

As the thrust coefficient increases, the bow shock standoff distance increases. For large values of thrust coefficient, the resultant flowfield becomes unsteady as the jets begin to disturb the bow shock[18] and the nozzle flow now diffuses through a terminal shock instead of mixing with the freestream[15]. Both Jarvinen and Adams[15,25] and Keyes and Hefner[26] observed local instabilities affecting the slope of the bow shock as the total thrust coefficient increased beyond approximately 3.0. However, the sharp increase in standoff distance and dissolution of the bow shock seen with the central nozzle configuration have not been observed with the peripheral nozzle configuration. Future work will be required to fully characterize the flowfield stability of configurations with peripheral nozzles.

IV. Aerodynamic Characteristics and Experimental Data Summary

The effects of supersonic retropropulsion flowfields on the aerodynamics of a blunt-bodied entry vehicle influence the configurations of retropropulsion desirable for EDL applications as a supersonic decelerator. The configuration of nozzles on the forebody and the ratio of the jet total pressure to the freestream total pressure govern the aerodynamic forces and static stability. Central and peripheral retropropulsion configurations exhibit fundamentally different flow behavior, resulting in contrasting aerodynamic effects.

A. Aerodynamic Characteristics

1. Central Retropropulsion Configurations

A substantial number of experiments were done from the late 1950s through the early 1970s on the aerodynamic effects of a centrally-located retronozzle for EDL applications. For blunt cones, hemispheres, and other bodies of revolution, at Mach numbers from 1.05 to 9, the results of these experiments indicate that the central retropropulsion configuration is unfavorable for use as a supersonic decelerator from an aerodynamic standpoint. References 15, 18-25, and 27-35 are all experimental investigations of central retropropulsion configurations.

With increasing thrust coefficient, the aerodynamic drag coefficient decreases rapidly to a minimum value of approximately 10% of the no-jet value and then remains constant at this minimum value. For thrust coefficients above approximately 0.4, the total axial force coefficient is dominated by the contribution from thrust. Above C_T ~0.8, the displacement of $C_{A,total}$ from C_T is roughly constant, with the displacement due to the minimally preserved aerodynamic drag. These effects are shown in Figure 6 (adapted[23]).
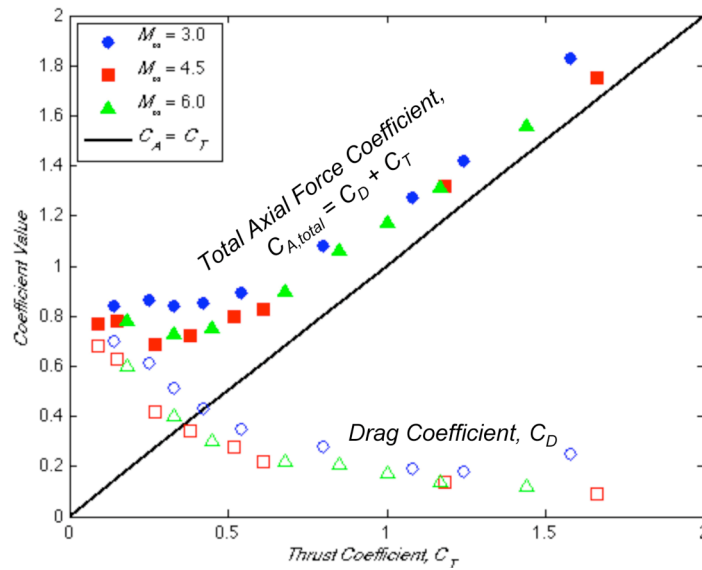

Figure 6. Aerodynamic Drag Coefficient Variation with Increasing Thrust Coefficient (adapted[23])

With flow from a central nozzle, the high stagnation pressure present in the no jet case is greatly reduced. The nozzle flow perturbs the bow shock to become more oblique than normal. This reduction in shock strength leads to a reduction in surface pressure, and subsequently aerodynamic drag[27]. The degree of these surface pressure reductions tends to increase as the freestream Mach number increases[23].

At thrust coefficients greater than approximately 0.2, the nozzle flow cannot be contained within the boundary layer, and a sharp flow turning angle causes the boundary layer to separate on both sides of the jet on the forebody. Strong recirculation regions form on both sides of the nozzle flow, moving the flow within the shock layer towards the vehicle's shoulder. Flow reattachment begins near a thrust coefficient of 2, and by higher thrust coefficients (at approximately $C_T = 6$), the base pressure of the body equals the forebody pressure, enveloping the body in a constant pressure region similar to wake flow[15,23]. Little variation in the surface pressure is seen between different blunt body geometries, indicating a relative independence of aeroshell cone angle on the drag reduction effects of central retropropulsion configurations.

Romeo and Sterrett[20] examined flowfield stability for a centrally-located jet over angles of attack from 0° to 35°. Beyond very small angles of attack (greater than 2°), the structure of the flowfield breaks down for total pressure

ratios (or thrust coefficients) corresponding to the case where the jet penetrates the bow shock and resulting standoff distance is large.

The pitching moment slopes for increasing thrust coefficients at freestream Mach numbers of 1.05 and 2.0 are shown in Figure 7[15]. The data were taken over angles of attack from -6° to +6°. For the central nozzle configuration, the pitching moment coefficient for a given thrust coefficient is nearly linear with variation in angle of attack (-6° to +6°). The pitching moment slope becomes increasingly negative as the thrust coefficient increases to 1, then becomes less negative with additional increases in thrust coefficient. The pitching moment slope is always negative, indicating that the entry body is statically stable. This static stability is observed even in cases where the flowfield itself may be unstable.
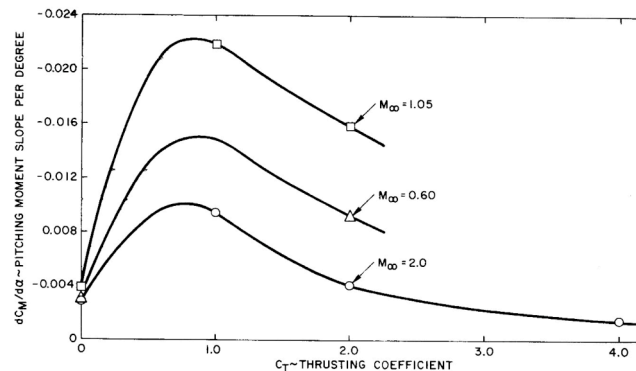

Figure 7. Variation of Pitching Moment Slope with Thrust Coefficient[15]

The severe reduction in aerodynamic drag contribution to the total axial force coefficient by centrally-located nozzle configurations is a drawback in this technology's application for supersonic deceleration. The flowfield stability transitions and observed flow unsteadiness over most freestream Mach numbers and thrust coefficients investigated are additional complications to the implementation of this configuration into an EDL architecture.

2. Peripheral Retropropulsion Configurations

From the standpoint of aerodynamic drag benefit, configurations where the nozzles are at the periphery of the forebody of a blunt entry vehicle are promising. Both Jarvinen and Adams[15,25] and Keyes and Hefner[26] experimentally observed augmentation of the total axial force coefficient at modest nozzle flow rates, a significant contrast to the reduction seen for configurations with retropropulsion along the body centerline. Experimental data has been taken at freestream Mach numbers of 1.05, 1.50, 2.0, and 6.0, using 60° sphere-cones, using air for the freestream and nozzle flow.

The lack of disruption of the center of the bow shock by the peripheral nozzle flow causes a region of high pressure to remain over portions of the aeroshell inboard of the nozzles, preserving the aerodynamic drag of the aeroshell[26]. The bow shock remains sufficiently undisturbed and close to the body for total thrust coefficients below 5.0[15].

Experimental work by Jarvinen and Adams[15,25] demonstrated a range of thrust coefficients over which a three-nozzle peripheral configuration (see Figure 5) provides substantially more total axial force than a single, centrally-located nozzle at the same total thrust coefficient. The comparison of total axial force coefficient between a peripheral nozzle configuration and a central nozzle configuration at the same conditions is shown in Figure 8[15].
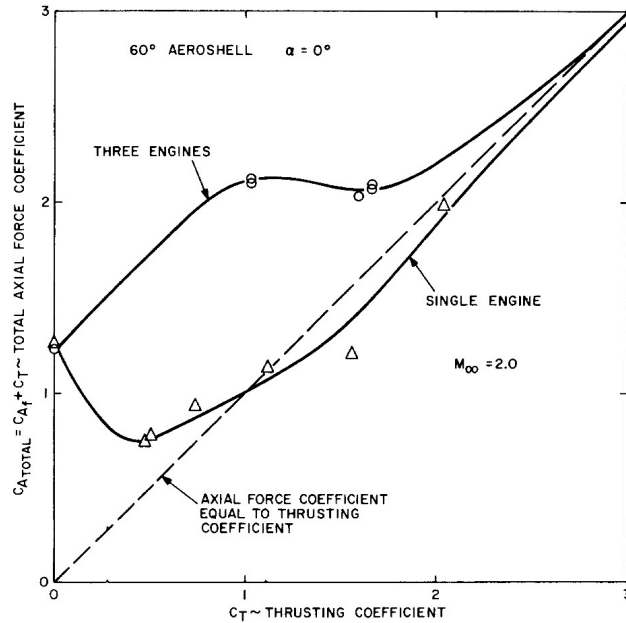
Figure 8. Comparison of Total Axial Force Coefficient for Peripheral and Central Configurations[15]

A configuration with three nozzles at the body periphery outperforms the configuration with a single central nozzle for thrust coefficients up to 2. At thrust coefficients above 2, the total axial force coefficients for both configurations are nearly equal to the thrust coefficient alone, given by the dashed line in Figure 8[15]. At lower thrust coefficients, the peripheral nozzle flow only mildly disturbs the bow shock at the edges. This perturbation flattens the bow shock at the edges, causing the flowfield to effectively see a larger blunt body. At higher thrust coefficients, the peripheral nozzle flow penetrates the bow shock, and the high pressure region inboard of the nozzles disappears as the bow shock weakens[15,26].

The augmentation of the total axial force coefficient is dependent on freestream Mach number. The maximum increase in total axial force coefficient, observed near a thrust coefficient of 1.0, increases over the freestream Mach numbers tested, likely due to the increasing strength of the bow shock[15]. In these cases, an axial force augmentation from aerodynamics approximately equal to the thrust force is possible. Surface pressure data confirms that the aeroshell surface is covered with a nearly uniform region of high pressure, and this surface pressure is highest at total thrust coefficients near 1.0[15].

Variation of angle of attack, from -6° to +6°, showed little effect on the forebody axial force coefficient for freestream Mach numbers 1.05, 1.50, and 2.0 with thrust coefficients from 0 to 1.9[15]. However, in contrast to the central nozzle configuration, the pitching moment coefficient exhibits nonlinear behavior, as shown in Figure 9[15]. For a thrust coefficient of 1.04 and Mach number of 2.0, the body is statically unstable at angles of attack between -2° and -8°. The varying nonlinearity and indiscernible dependence on thrust coefficient causes difficulty in determining a trend in static stability with increasing thrust coefficient with the limited data available for the peripheral configuration.

The marked increase in the total axial force coefficient for low to modest thrust coefficients make peripheral retropropulsion configurations favorable for EDL applications as a supersonic decelerator. The maximum augmentation in total axial force occurs at total pressure ratios (equivalently low thrust coefficients) typical of stable flowfields. However, the existing experimental database for peripheral configurations is limited, suggesting a need to expand the database to additional configurations and conditions for accurate comparison between peripheral retropropulsion configurations and alternative supersonic decelerator technologies.
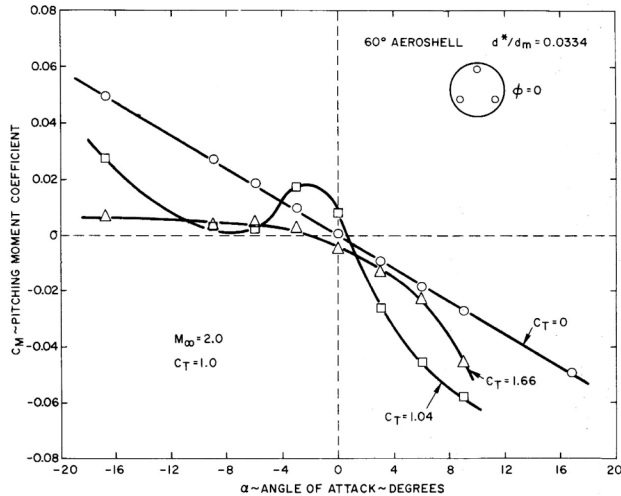
Figure 9. Variation of Pitching Moment Coefficient with Thrust Coefficient and Angle of Attack[15]

3. Differential Throttling Effects

Jarvinen and Adams[15,25] also explored drag modulation capability by throttling combinations of three engines of a peripheral retropropulsion configuration. The amount of variation in total axial force coefficient between throttled and unthrottled conditions was observed to increase with increasing freestream Mach number. At a freestream Mach number of 1.05, little variation between the no throttling case and cases where one engine was throttled down by 50% and 75% was observed at thrust coefficients below 3.0. However, in a Mach 2.0 freestream, significant variation between the two cases was observed at total thrust coefficients above 1.0.

Similar departures were observed under the same conditions for cases where two of the three engines were throttled down[15]. In the $M_\infty = 1.05$ case, with one engine throttled down by 50% and the total thrust coefficient increased from 0.5 to 3.0, the forebody drag coefficient decreased from 0.8 to approximately zero. At the same freestream conditions, with two engines throttled down and the thrust coefficient increased from 0.5 to 3.0, the forebody drag coefficient decreased from 0.8 to approximately -0.4. In the $M_\infty = 2.0$ case, with one engine throttled down and the thrust coefficient increased from 0.5 to 3.0, the forebody drag coefficient decreased from 1.2 to approximately -0.1. In the $M_\infty = 2.0$ case, with two engines throttled down and the thrust coefficient increased from 0.5 to 3.0, the forebody drag coefficient decreased from 1.2 to approximately 0.1. Jarvinen and Adams[15] concluded that as freestream Mach number increased, the same degree of forebody drag coefficient modulation could be realized with decreasing thrust coefficients.

Throttling combinations of engines at the body periphery also produced alterations in the static stability of the vehicle[15]. The total pitching moment on the body is the sum of the pitching moment due to surface pressure forces and the pitching moment induced by imbalances in thrust. In cases where the blunt body was oriented at a positive angle of attack, throttling down engines on the leeward side of the forebody induced a nose-down pitching moment. In the same orientation, throttling down engines on the windward size of the forebody induced a nose-up pitching moment.

These induced pitching moments can be attributed to the asymmetry of the detached bow shock, a condition arising from the non-uniform engine thrust and resulting total axial force changes at throttled conditions. Schlieren images[15] show an increase in standoff distance and an increase in the obliqueness of the local section of the bow shock in the region of the unthrottled nozzle flow. The decrease in shock strength with the increase in obliqueness support the conclusion that the reduction in axial force coefficient with increasing thrust coefficient is strongly dependent on changes to the surface pressure distribution caused by throttling. The effectiveness of throttling in controlling pitching moment, defined as the ratio of change in pitching moment measured experimentally to the change in pitching moment due solely to an imbalance in engine thrust, was observed to be reduced by 20% at supersonic freestream conditions as compared to throttling efficiency at subsonic velocities. Jarvinen and Adams[15,25] attributed this reduction in throttling effectiveness to the effect of supersonic freestream conditions on the total axial force coefficient.

B. Experimental Summary

The focused technology development program for planetary exploration in the 1960s and early 1970s matured supersonic retropropulsion close to its current level of readiness through a number of experimental investigations. The intent of these experiments was to understand drag effects potentially advantageous to EDL. Scaling parameters were developed to accurately simulate the larger chemical bipropellant propulsion systems visualized for conceptual Mars landers using subscale models. However, to date, only monopropellant descent propulsion systems have been flown. No work has been found in support of missions to destinations other than Mars.

1. Simulation Parameters for Similarity and Scaling

Pindzola[43] developed methods for simulating nozzle flow using ground facilities and selecting geometries and test conditions to account for differences in chemical species properties between models and full scale. Primary jet flow parameters are governed by relations to nozzle mass flow, enthalpy, and momentum. Jarvinen and Adams[15,25,31] extended Pindzola's methods for accurately simulating jet flows in a wind tunnel to the retrorocket exhaust of a conceptual Mars lander. The freestream Mach number, thrust coefficient, plume sensitivity parameter, and engine scaling parameter are the scaling parameters matched for proper simulation of retrorocket flow at subscale in a wind tunnel.

The nozzle exhaust flow is simulated by matching the ratio of pressure at the nozzle exit to the ambient pressure and the pressure sensitivity of the exhaust flow with respect to the flow direction, given by Equation 2, where P is the pressure and v is the flow direction at the nozzle exit plane. Equation 2 is also known as the plume sensitivity parameter[15,43].

$$Plume\ sensitivity\ parameter = \frac{1}{P}\frac{dP}{dv} \tag{2}$$

The thrust coefficient, given previously by Equation 1, is the primary parameter governing the interaction between nozzle flow and an opposing supersonic freestream. The thrust coefficient can be rewritten in terms of both freestream and nozzle flow parameters, shown by Equation 3[15] where A_B is the model base area, A_e is the nozzle exit area, and γ_∞ and γ_e are the ratio of specific heats of the freestream and at the nozzle exit, respectively.

$$C_T = \frac{2}{\gamma_\infty M_\infty^2}\frac{P_e}{P_\infty}\frac{A_e}{A_B}\left(1+\gamma_e M_e^2\right) \tag{3}$$

Rearranging Equation 3 to have all freestream parameters except γ_∞ on the left-hand side and all nozzle flow parameters on the right-hand side gives the engine scaling parameter, defined by Equation 4[15].

$$Engine\ scaling\ parameter = \frac{\gamma_\infty A_B}{2A_e\left(1+\gamma_e M_e^2\right)} \tag{4}$$

2. Existing Experimental Database

While numerous wind tunnel tests were conducted, the scope of the work was limited in terms of freestream conditions, retropropulsion conditions, and body geometries. The majority of past efforts focused on blunt bodies with a single, centrally-located nozzle – a configuration which does not appear to be favorable for supersonic deceleration applications due to the resulting significant reduction in the aerodynamic drag of the blunt body. Only three investigations have been found that utilized multiple nozzles[15,24,25]. An additional limitation of the existing data is the use of compressed air, nitrogen, hydrogen, or helium in all test cases for the nozzle exhaust. No experimental data exists in which combustion products were exhausted, possibly due to test scale and the complexity of combustion systems. In addition, the primary goal of most of these investigations was to explore potential reductions in heat transfer, not deceleration. A summary of the flow conditions and geometries comprising the existing experimental database are summarized in Table 3.

Table 3. Existing Experimental Database

3a. Available Central Nozzle Configuration Data

Relevance	Freestream Mach	Freestream	Jet	References
Static Aerodynamics	1.05 - 6.0, 20 - 21	Air	Air, Helium	[15],[18]-[21],[23]-[25],[27]-[29],[31]-[35],[37],[39]-[41],[44]
Flowfield Stability	1.05 - 6.0	Air	Air, Helium	[15],[18],[23]-[25],[27],[37]
Flowfield Geometry	1.05 - 8.0	Air	Air, Helium	[15],[18]-[21],[23]-[25],[28]-[29],[31]-[34],[40]
Effect of Nozzle Geometry	1.05 - 6.0, 20 - 21	Air	Air, Helium	[15],[18],[20]-[21],[25],[31],[39],[41]
Angle of Attack Variation	1.05 - 6.0	Air	Air, Helium	[15],[20],[23]-[25]
Aerothermodynamics	2.0, 6.0 - 8.0, 20 - 21	Air	Air, Helium, Nitrogen, Hydrogen	[19],[21],[34]-[42],[45]
Systems-Level Implications	1.05 -6.0	Air	Air	[15],[20],[25],[27],[41]

3b. Available Peripheral Nozzle Configuration Data

Relevance	Freestream Mach	Freestream	Jet	References
Static Aerodynamics	1.05 - 6.0	Air	Air	[15],[25]-[26]
Flowfield Stability	1.05 - 2.0	Air	Air	[15],[25]
Flowfield Geometry	1.05 - 2.0	Air	Air	[15],[25]-[26]
Effect of Nozzle Geometry	1.05 - 2.0	Air	Air	[15],[25]
Angle of Attack Variation	1.05 - 2.0	Air	Air	[15],[25]
Aerothermodynamics	None	N/A	N/A	N/A
Systems-Level Implications	1.05 - 2.0	Air	Air	[15],[25]-[26]

This experimental database will need to be expanded to include additional retropropulsion configurations, body geometries, exhaust and freestream species, combustion retropropulsion, and a broader range of flow conditions. Slender body geometries such as biconics and ellipsleds are candidates for human Mars architectures, and no data exists to validate computational simulation of supersonic retropropulsion systems derived for these geometries. As the work by Peterson and McKenzie[24] is the only configuration of multiple nozzles not located on the body periphery, data on the required nozzle spacing to prevent an interaction between exhaust jets is also unknown.

V. Computational Analyses in the Literature

Few papers have been published on the computational modeling and analysis of supersonic retropropulsion. Recent work has focused on drag reduction for slender body vehicles, not drag augmentation for blunt bodies, and the effects of high temperature plasma jets on the body aerodynamics[44,45]. However, the similarities in flowfield interactions between these applications and supersonic retropropulsion for EDL have been useful in extending computational approaches.

Computational solutions of supersonic retropropulsion systems may need to capture the following characteristics:

- Flow features such as strong shocks, shock/boundary layer interactions, shock-shock interactions, and recirculation.
- Viscous effects within the shock layer.
- Relevant equilibrium and nonequilibrium chemistry.
- Diffusion and transport properties of the exhaust flow.
- Radiative energy transfer in the flow, if necessary.

Additionally, oscillatory behavior, makes starting solutions and convergence difficult. Despite these challenges, several recent studies[21,37,44,45] have shown some success in modeling the aerothermodynamics of single nozzle configurations.

Daso, et al.[21] completed pre-test computational fluid dynamics (CFD) analysis with a 2.6% scale model of the Apollo capsule with and without retropropulsion effects. The CFD analysis was attempting to predict the aerodynamic and aerothermodynamic effects of a centrally-located nozzle in air at freestream Mach numbers of 3.48 and 4.0. Both the pre-test computational simulations and associated experiment used compressed air for the nozzle exhaust[21]. While little attention is presented on the details of the CFD analysis, the use of a 3-D structured grid

Navier-Stokes solver predicted the transitions in flow stability and captured the general aerothermodynamic trends observed in subsequent testing. The characteristic unsteadiness and oscillatory behavior of the flowfields with retropropulsion resulted in asymmetric flowfield geometries.

Fomin and Maslov[44] performed numerical simulations in support of experimental work on the blunt-body pressure effects of a centrally-located high temperature plasma jet at freestream Mach numbers of 2.0, 2.5, and 4.0. Composition of the freestream was air, and the plasma jet was nitrogen gas at 5000 K. Experimental results were compared against an Euler CFD analysis in an effort to understand the separation existing between fluid dynamics and the thermal processes in a supersonic freestream-propulsion interaction. The Euler solver was able to capture the reduction in body surface pressures caused by transition to unstable flow and jet penetration of the bow shock. The relatively good agreement seen between the Euler solutions and the experimental plasma jet work suggests much of the interactions at supersonic Mach numbers resemble retropropulsion gas dynamics, a result promising for future work focused on inclusion of combustion products[44]. Additional work[45] from the same authors has been reported in which supersonic retropropulsion in the form of plasma jets is modeled using the assumption of a perfect gas with constant specific heats.

Hayashi, et al.[37] solved the axisymmetric Navier-Stokes equations to predict reductions in aerothermal heating in the stagnation region of a hemisphere at a freestream Mach number of 3.96. Freestream composition was air, and the nozzle exhaust was nitrogen gas at 300 K. The CFD results showed good agreement with experiment, particularly in the ability to capture the recirculation regions about a centrally-located jet. The strength of the recirculation regions was slightly higher than observed experimentally, resulting in more efficient heat flux reduction in the CFD solution than observed in the experiment.

Computational simulation of the interactions between retronozzles and supersonic freestreams is the next phase of investigation required to mature supersonic retropropulsion from a potentially feasible concept to a useful EDL technology. The ability of preliminary CFD investigations to capture trends in surface pressure, flowfield geometry, and patterns of heat flux, despite unsteadiness and oscillatory behavior, is encouraging for the continued development of approaches for high-fidelity computational modeling. While these preliminary efforts are good first steps in developing computational capability, much of the physics relevant to the behavior of supersonic retropropulsion is coupled and viscous in nature. Flow separation, recirculation, boundary layer transition, and oscillation of the position of primary flow features such as the detached bow shock, free stagnation point, and jet flow boundary are relevant characteristics of supersonic retropropulsion flowfields. Computational solutions that accurately capture these characteristics exist under a very limited range of conditions at this point.

VI. Concluding Remarks from Literature Review

Interactions between retropropulsion exhaust and blunt body aerodynamics have been investigated since the early 1950s. Extensive wind tunnel experiments in the 1960s and early 1970s developed the technology to near the level of maturity it has today. Experimental results consistently show, significant axial force benefits (aerodynamic augmentation to thrust) for peripheral retropropulsion configurations at low thrust coefficients. The literature also demonstrates little or no aerodynamic axial force augmentation beyond that provided by the retrorocket thrust for configurations with the nozzle located along the body centerline. The degree of aerodynamic interaction is strongly dependent on the location of the nozzles and the relative strength of the exhaust flow to the freestream. The primary parameter used to characterize the static aerodynamics and flowfield stability is the thrust coefficient, with the greatest degree of axial force augmentation for peripheral retropropulsion configurations occurring near a thrust coefficient of 1.0.

Despite the extensive focus on retropropulsion in the 1960s and early 1970s, significant limitations exist in the current experimental database. The most significant challenges in maturing supersonic retropropulsion are related to a lack of knowledge in the following areas:

- Configurations with nozzles at the body periphery.
- Aerodynamic interactions on slender body vehicle geometries.
- Aerothermal effects caused by exhausting combustion products into the shock layer.
- Uncertainties in scaling wind tunnel results to flight systems.
- Validated computational fluid dynamic approaches.

VII. Preliminary Systems-level Assessment of Supersonic Retropropulsion

Past experimental work has shown supersonic retropropulsion to be physically possible on a small scale, establishing trends in static aerodynamics as a function of retropropulsion configuration, freestream conditions, and thrust effort. However, prior high mass Mars EDL systems studies have neglected propulsive-aerodynamic interactions and performance impacts during the supersonic phase of descent. The broad goal of this study is to accurately evaluate the performance of supersonic retropropulsion with increasing vehicle ballistic coefficient across a range of initiation conditions. Results are presented with the potential aerodynamic augmentation included and excluded during this phase of flight for comparison against prior studies. The parametric analysis performed varied retropropulsion initiation conditions (Mach number and altitude) and required thrust coefficient for ballistic coefficients ranging from 100 to 500 kg/m^2. The model developed propagates the trajectory from the supersonic retropropulsion initiation conditions until the vehicle reaches subsonic conditions (Mach 0.9).

A. Models and Methods

1. Atmosphere Model

The atmosphere model was developed by Seiff[46] following the Viking lander missions in the 1970s. The model is given in the reference as tabulated data on temperature, pressure, density, and gravity as a function of altitude, up to 100 km. The Seiff atmosphere model used is for the Northern hemisphere in the summer season at latitudes below 60°. The surface density at 0 km is 1.56x10^{-2}kg/m^3. All atmosphere conditions at altitudes below 0 km are assumed to be equivalent to conditions at 0 km. 0 km is defined relative to the Mars reference ellipsoid developed by Christensen in 1975[47]. The surface conditions (conditions given for 0 km) were determined by translating surface measurements from Viking 1 (-1.5 km), Viking 2 (-2.5 km), and Mars 6 (+1.3 km) to equivalent conditions on the reference ellipsoid.

2. Vehicle Configuration

The vehicle was assumed to be an Apollo-like capsule (32° sidewall angle, C_D = 1.3) with three bipropellant engines at the periphery of the forebody, as shown in Figure 10. Past work by Christian, et. al.[12] showed that for a blunt entry body, a propulsive configuration with the engines towards the forebody periphery provides more useful volume for payload and propellant tanks than a cluster of engines at the center. The propulsion system was assumed to be LOX/CH$_4$ with an I_{sp} of 350 seconds. No other assumptions were made about the configuration of the entry vehicle.

Figure 10. Retropropulsion Configuration and Aeroshell Geometry[12]

3. Trajectory Model

From a specified set of initiation conditions (altitude, mass, Mach number, flight path angle), the trajectory is propagated toward the ground until vehicle reaches Mach 0.9, the preliminary terminal condition for this study. The initial flight path angle was assumed to be -8.5° and used as the initial flight path angle for all cases. A spherical, rotating planet is assumed, as the vehicle is likely to travel significant downrange distances during supersonic descent. Mars and its atmosphere were assumed to rotate with constant angular velocity, ω. The vehicle is fixed at zero angle of attack; no lift is generated. The 3-DOF governing equations for a point mass entry vehicle traveling over a spherical, rotating Mars with a constant retropropulsive thrust can be written as[48]:

$$\frac{dr}{dt} = V \sin \gamma \quad (5)$$

$$\frac{d\theta}{dt} = \frac{V \cos \gamma \cos \psi}{r \cos \phi} \quad (6)$$

$$\frac{d\phi}{dt} = \frac{V \cos\gamma \sin\psi}{r} \tag{7}$$

$$\frac{dV}{dt} = \frac{1}{m} F_T - g\sin\gamma + \omega^2 r \cos\phi \left(\sin\gamma\cos\phi - \cos\gamma\sin\phi\sin\psi\right) \tag{8}$$

$$V\frac{d\gamma}{dt} = \frac{1}{m} F_N \cos\sigma - g\cos\gamma + \frac{V^2}{r}\cos\gamma + 2\omega V \cos\phi\cos\psi + \omega^2 r \cos\phi\left(\cos\gamma\cos\phi + \sin\gamma\sin\phi\sin\psi\right) \tag{9}$$

$$V\frac{d\psi}{dt} = \frac{1}{m}\frac{F_N \sin\sigma}{\cos\gamma} - \frac{V^2}{r}\cos\gamma\cos\psi\tan\phi + 2\omega V\left(\tan\gamma\cos\phi\sin\psi - \sin\phi\right) - \frac{\omega^2 r}{\cos\gamma}\sin\phi\cos\phi\cos\psi \tag{10}$$

$$\frac{dm}{dt} = -\frac{T}{I_{sp}g_E} \tag{11}$$

$$F_T = -T\cos\varepsilon - D \tag{12}$$

$$F_N = T\sin\varepsilon + L \tag{13}$$

Equations (5) – (7) are the kinematic equations of motion, yielding time derivative information for the radial distance from the planet center, longitude, and latitude. Equations (8) – (11) are the force equations, yielding time derivative information for velocity, flight path angle, heading angle, and vehicle mass. Equations (12) and (13) are expressions for normal and tangential force components arising from thrust, lift, and drag. Longitude is measured from the x-axis in the equatorial plane, positively eastward. Latitude is measured from the equatorial plane along a meridian, positively northward. Flight path angle is positive when the velocity is above the local horizontal plane. Heading angle is measured positively in the right-hand direction about the x-axis. The planetary constants used are given in Table 4.

Table 4. Mars Planetary Constants

Equatorial radius, r_0 (km)	3396.2
Surface gravitational acceleration, g_0 (m/s^2)	3.718
Surface density, ρ_0 (kg/m^3)	1.56x10^{-2}
Planetary rotation rate, ω (rad/s)	7.0882x10^{-5}

4. Supersonic Retropropulsion Propulsive-Aerodynamic Interactions Model

The aerodynamics model is based primarily on experimental multiple nozzle work by Jarvinen and Adams[15] and assumes a peripheral retropropulsion configuration (Figure 5Figure 8). Past experimental work suggests such a configuration will preserve aerodynamic drag during the retropropulsion phases, an effect not observed for configurations with an engine or cluster of engines at the center[15,20,23,24,25]. The aerodynamics model takes the required deceleration force coefficient as an input, for either a fixed thrust coefficient or a thrust coefficient determined from preset terminal conditions, and outputs the required total axial force coefficient (summing aerodynamic and propulsive effects). While the current form of the model does not include Mach number variations in determining aerodynamics, McGhee[23], with Jarvinen and Adams[15,25] and Keyes and Hefner[26], observed only minor variations in static aerodynamic force coefficient for initiation Mach numbers between 2.0 and 6.0. Individual cases must require a deceleration force greater than the aerodynamic drag provided by the blunt body for the propulsive model to be called. For thrust coefficients above 3.0, the deceleration force coefficient is equivalent to the thrust coefficient and no aerodynamic adjustment to the thrust coefficient is applied.

5. Mass Model

Based on the ballistic coefficient for each case, the vehicle mass at retropropulsion initiation is determined. During the retropropulsion phase, vehicle mass is included in the state, updated at each time step using Equation 11. As this study is only concerned with the supersonic retropropulsion phase of the trajectory, no other sizing relations

are included. Propellant mass required and vehicle entry mass are used to determine the supersonic descent propellant mass fraction for comparison.

6. Methods

These models (atmosphere, aerodynamics, vehicle configuration, trajectory, and mass) are all developed in MATLAB, with the equations of motion integrated using the ODE45 solver. User-specified vehicle characteristics, retropropulsion initiation conditions, thrust coefficient, and terminal conditions are required to run the integrated model. Based on past system study results of the hypersonic flight phase, supersonic retropropulsion initiation conditions were varied from Mach 1.5 to Mach 6.0 for altitudes of 5 km to 15 km. Thrust coefficient was varied from 1.5 to 3.0 for each case. Ballistic coefficient was varied from 100 kg/m^2 to 500 kg/m^2. Initial flight path angle was -8.5º for all cases; no flight path angle sweeps were considered.

B. Systems Study Results

This section presents the results of a preliminary systems level assessment of supersonic retropropulsion, defining relationships between vehicle ballistic coefficient, initiation conditions (altitude and Mach number), final altitude, and supersonic descent propellant mass fraction. Approximate limits on the maximum ballistic coefficient for significant aerodynamic-propulsive interaction are also defined. The following table gives approximate vehicle entry masses corresponding to the ballistic coefficients used in this study for 10, 12, and 15 m diameter Apollo-derived aeroshells:

Table 5. Entry Masses (kg) for Various Diameter Aeroshells

	10 m	12 m	15 m
β = 100 kg/m^2	10200	14700	23000
β = 150 kg/m^2	15300	22000	34500
β = 200 kg/m^2	20400	29400	46000
β = 250 kg/m^2	25500	36700	57500
β = 300 kg/m^2	30600	44100	68900
β = 350 kg/m^2	35700	51400	80400
β = 400 kg/m^2	40800	58800	91900
β = 450 kg/m^2	45900	66200	103300
β = 500 kg/m^2	51000	73500	114800

The majority of the results presented assumed a fixed thrust coefficient, C_T, to determine the thrust magnitude for each case. Equation 1 gives C_T to be a function of the dynamic pressure, q_∞, and the reference area, A (the base area of the aeroshell). As a result of fixing thrust coefficient and not thrust magnitude, the thrust magnitude is proportional to atmospheric density, decreasing with decreasing density (or equivalently, decreasing with increasing initial altitude). The thrust magnitude used for propagating each trajectory is found with the following relation:

$$T = \rho_\infty \left(\frac{1}{2} C_T V_\infty^2 A \right) \tag{14}$$

For each ballistic coefficient, the retropropulsion initiation altitude was varied from 5 km to 15 km. The progression of points forming the contours on the following plots represents the range of initiation altitudes for a given case. Initiation altitudes not included within the 5 – 15 km range on the following series of plots were cases where insufficient atmospheric density required unrealistic initiation conditions or resulted in an unacceptable terminal state. The dependence of the thrust magnitude on atmospheric density caused the higher initiation altitudes to be correlated with the lower terminal altitudes. In a more tangible sense, for $C_T = 2.0$ and $M_{init} = 3.0$, retropropulsion initiation at 5 km corresponds to a thrust magnitude of 836.6 kN; initiation at 10 km corresponds to a thrust magnitude of 528.9 kN; initiation at 15 km corresponds to a thrust magnitude of 327.1 kN.

1. Effect of Varying Ballistic Coefficient

Figure 11 shows the effect of increasing ballistic coefficient on propellant mass fraction (PMF) and terminal altitude (Mach 0.9) for $C_T = 2.0$ and retropropulsion initiation at Mach 3.0. $C_T = 2.0$ was chosen to show performance trends with increasing ballistic coefficient for a moderate thrust magnitude with significant aero-propulsive interaction effects. While the aerodynamic drag contribution to the total axial force is greater for lower thrust coefficients, the corresponding thrust magnitudes are often too low to yield reasonable subsonic terminal states. Each individual point represents a different initiation altitude for each ballistic coefficient, as indicated in the figure. As expected, the lowest ballistic coefficient cases have the lowest propellant mass fractions and the highest terminal altitudes. These specific initiation conditions result in acceptable terminal altitudes (greater than 3 km) for ballistic coefficients up to 300 kg/m². For a fixed thrust coefficient and initiation Mach number, the propellant mass fraction appears to be dependent only on the ΔV required.

Each β contour shows the effect of fixing thrust coefficient and not thrust magnitude as the initiation altitude was varied. At lower initiation altitudes, the vehicle has less time to decelerate to subsonic conditions, but the atmospheric density is higher. At higher initiation altitudes, the vehicle has more time to decelerate, but the atmospheric density is lower, resulting in a lower thrust magnitude for a fixed thrust coefficient. At the median initiation altitudes, the vehicle has more time to decelerate than the lowest initiation altitude cases and a denser atmosphere than the highest initiation altitude cases, a combination resulting in the highest terminal altitudes. For the lowest ballistic coefficient cases ($\beta = 100$ kg/m², $\beta = 150$ kg/m²), the limited time to decelerate is overshadowed by the permissible thrust magnitude, resulting in the effect of fixing thrust coefficient being much more significant for the higher ballistic coefficient cases.
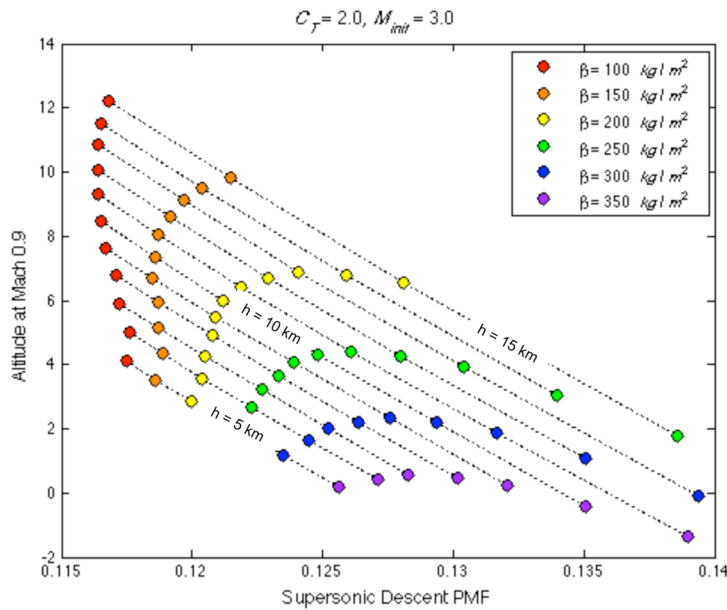

Figure 11. Effect of Increasing Ballistic Coefficient, Aero-Propulsive Effects Included

Figure 12 illustrates the significance of including the aero-propulsive interactions inherent with supersonic retropropulsion on descent propellant mass fraction for several ballistic coefficients. For the same initiation conditions, the performance difference in propellant mass fraction is consistent across all four ballistic coefficients. For fixed initiation conditions, ballistic coefficient does not impact the deceleration performance of supersonic retropropulsion.
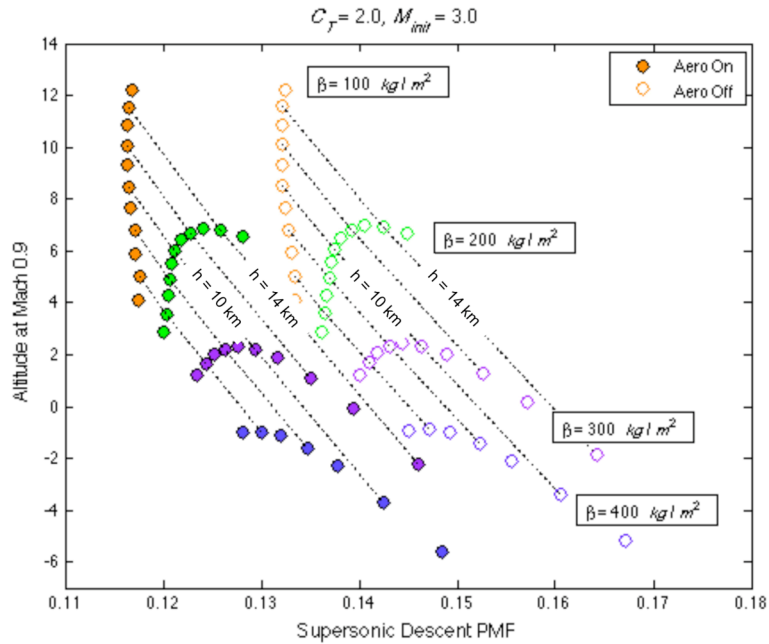
Figure 12. Significance of Aero-Propulsive Interactions with Ballistic Coefficient

1. Effect of Varying Initiation Mach Number and Altitude
    The effect of varying retropropulsion initiation conditions (Mach number and altitude) was explored for a low ballistic coefficient case and a high ballistic coefficient case. Both cases are for a fixed thrust coefficient of 2.0. Contours of initiation Mach number for the low ballistic coefficient case ($\beta = 100$ kg/m^2) are given in Figure 13, and similar contours for the high ballistic coefficient case ($\beta = 400$ kg/m^2) are given in Figure 14.
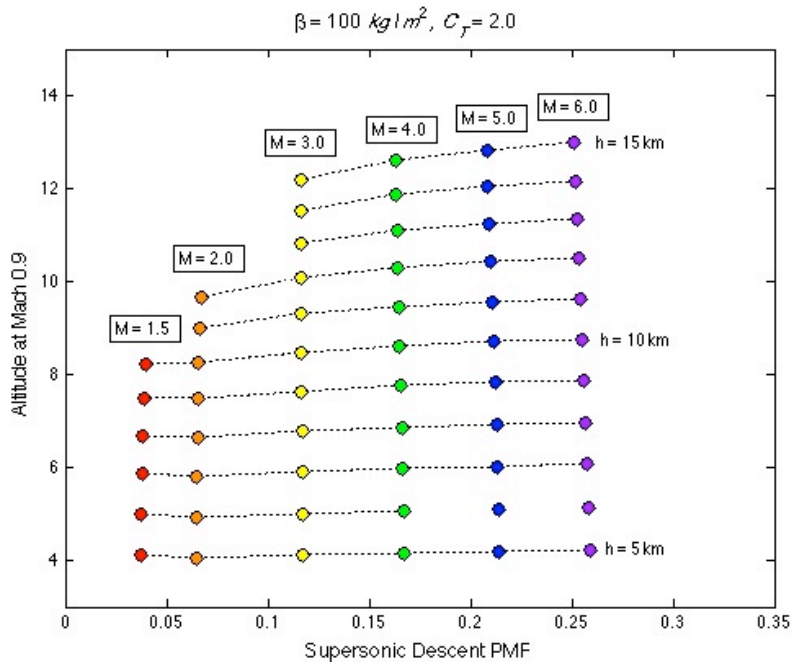

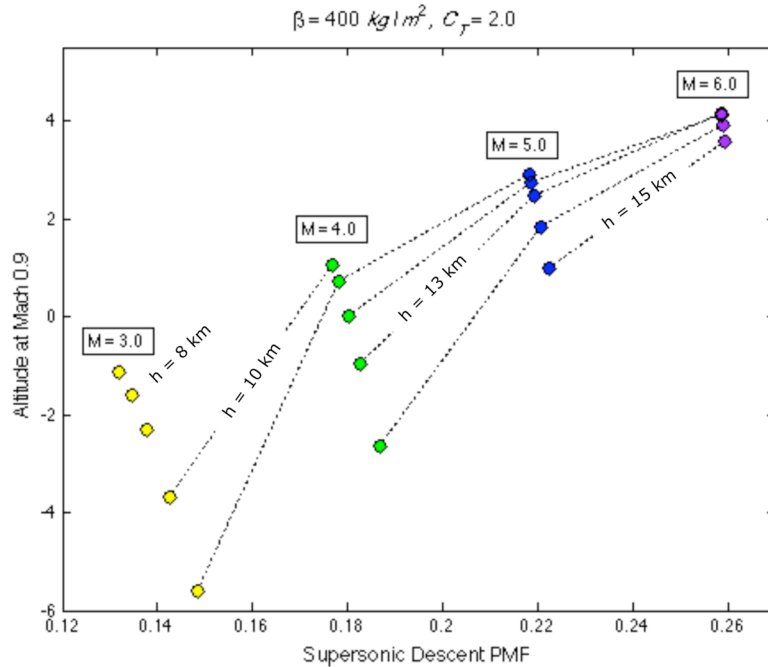Figure 13. Effect of Varying Initiation Conditions, Low Ballistic Coefficient Case

Figure 14. Effect of Varying Initiation Conditions, High Ballistic Coefficient Case

As expected, higher initiation Mach numbers and initiation altitudes result in higher terminal altitudes. Initiating retropropulsion earlier in the trajectory requires more propellant to reach subsonic conditions as the model assumes a constant thrust magnitude for a given trajectory (from a fixed C_T). In each case, to minimize propellant mass fraction, one would choose to initiate supersonic retropropulsion as late in the trajectory as possible. Figure 14 shows a clustering of points towards the lower initiation altitudes and higher initiation Mach numbers. Many of these high ballistic coefficient do not achieve the required subsonic terminal conditions until an altitude below 0 km. Because the atmosphere model uses the 0 km density for all altitudes below 0 km, this clustering appears (follow on work will replace the atmosphere model and regenerate Figures 14 and 16 to eliminate this clustering). For a fixed ballistic coefficient and thrust coefficient, the propellant mass fraction again appears to be largely a function of the required ΔV to reach the desired terminal conditions (Mach 0.9).

Figure 15 and Figure 16 show the increasing performance impact of supersonic retropropulsion as a function of initiation conditions for $\beta = 100$ kg/m^2 and $\beta = 400$ kg/m^2, respectively. The difference in descent propellant mass fraction between cases including the aerodynamic interactions and cases which neglect these aerodynamics increases with initiation Mach number. Increasing initiation altitude does not show any effect. The high ballistic coefficient case shows a larger difference between "aero effects on" and "aero effects off". The assumption of a constant thrust magnitude over the entire trajectory, with the same reduction in required thrust coefficient (as compared to the actual thrust coefficient to achieve the same total deceleration force) applied in each case, causes this amplification with increasing initiation Mach number. The increase in required ΔV with ballistic coefficient translated into higher descent propellant mass fractions.
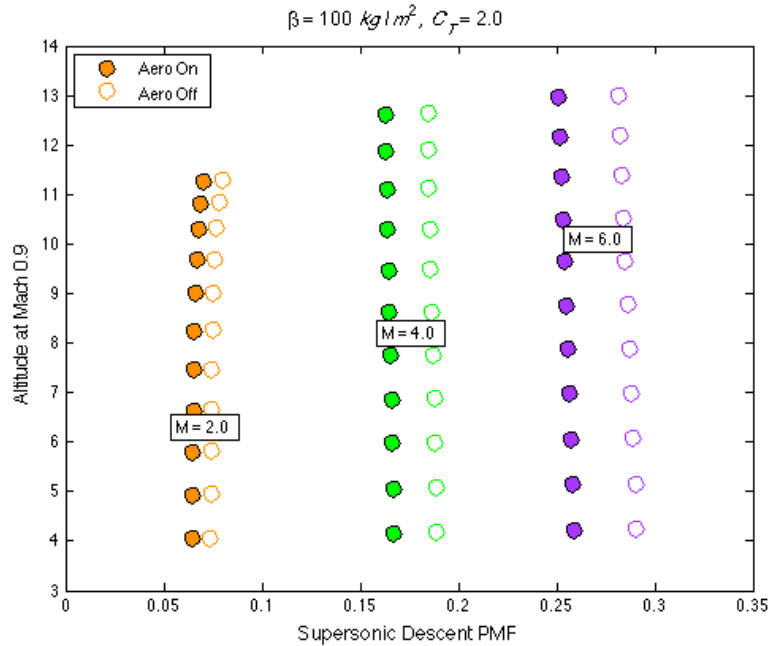
Figure 15. Significance of Aero-Propulsive Interactions for Varying Initiation Conditions
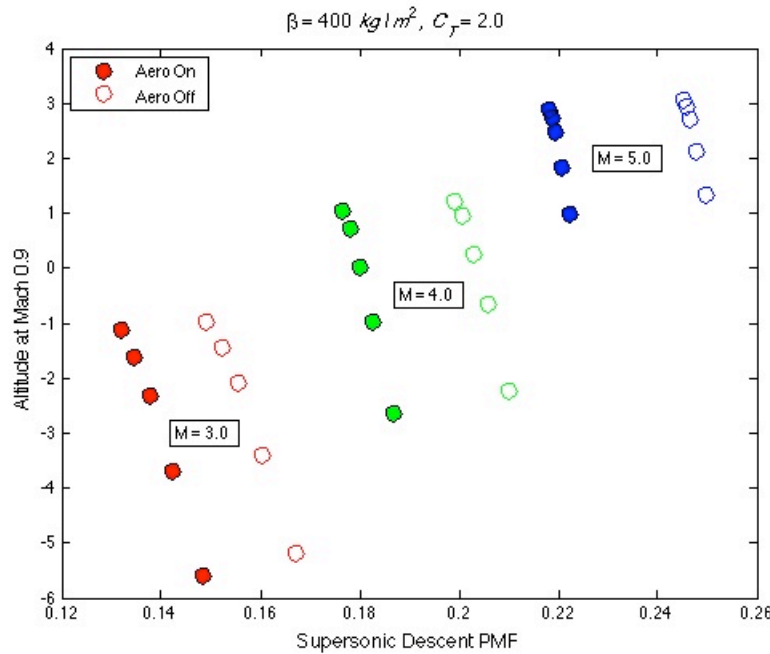

Figure 16. Significance of Aero-Propulsive Interactions with Varying Initiation Conditions

2. Effect of Varying Thrust Coefficient

Figure 17 shows the effect of varying C_T from 1.0 (maximum effect of aero-propulsive interactions) to $C_T = 3.0$ (no effect due to aero-propulsive interactions). Each point on the C_T contours corresponds to a different initiation altitude, ranging from 5 to 15 km. The constant C_T effect described earlier is evident in Figure 17 with the peaking of the terminal altitude at a median initiation altitude. As expected, the terminal altitude attainable for $\beta = 200$ kg/m^2 and retropropulsion initiation at Mach 2.0 increases with thrust coefficient. Higher required ΔV's and thrust magnitudes (from a higher C_T) correspond to higher required descent propellant mass fractions. The increase in

terminal altitude with thrust coefficient for little change in propellant mass fraction is a result of decreasing benefit from aero-propulsive interactions as thrust coefficient increases. Increasing thrust magnitudes with increasing thrust coefficient shift the terminal altitudes higher.

Figure 18 shows the performance impact of aero-propulsive interactions decreases with increasing C_T, a result in agreement with experimental work by Jarvinen and Adams[15,25] and the use of an aero-propulsive interaction model developed from this work. The maximum effect of the aero-propulsive interactions is near $C_T = 1.0$. The aero-propulsive interactions steadily decrease in strength with increasing thrust coefficient, bounded by an upper limit of $C_T = 3.0$. No axial force augmentation (due to aerodynamic effects) has been observed for C_T above ≈ 3.0.
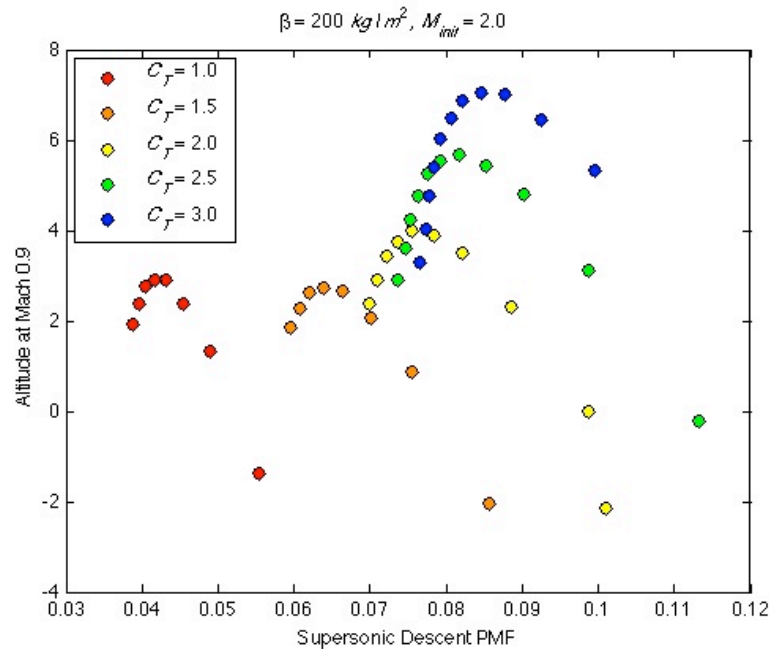

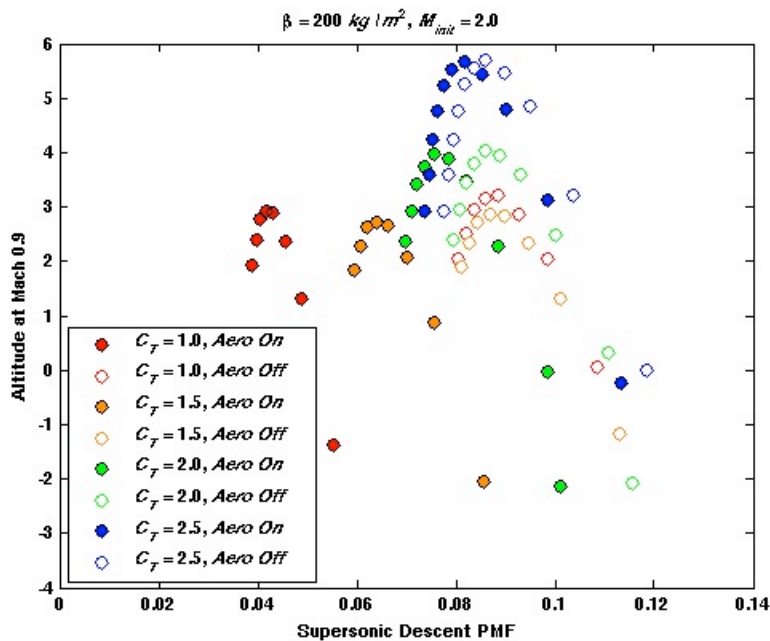Figure 17. Effect of Varying Thrust Coefficient, Aero-Propulsive Effects Included

Figure 18. Significance of Aero-Propulsive Interactions with Varying C_T

3. Ballistic Coefficient Limit for Significant Aerodynamic Effects

An approximate ballistic coefficient upper bound can be computed as a function of thrust coefficient by identifying the maximum ballistic coefficient for which the vehicle can reach Mach 0.9 at 3 km altitude or higher without requiring retropropulsion initiation above Mach 5.0. Initiation Mach numbers above ~5 are assumed to be at the upper limit of supersonic conditions. These limits are related to thrust coefficient as a balance between thrust magnitude and the strength of the aero-propulsive interactions. Table 6 gives the approximate ballistic coefficient limits for thrust coefficients ranging from 1.0 to 3.0 and the corresponding C_D reduction and supersonic propellant mass fraction.

Table 6. Approximate Ballistic Coefficient Limits for Mach 5.0 Supersonic Retropropulsion Initiation

	C_D	$C_{A,total}$	β (kg/m^2)	PMF
$C_T = 1.0$	~ 1.1	~ 2.1	350	0.124
$C_T = 1.5$	~ 0.6	~ 2.1	350	0.184
$C_T = 2.0$	~ 0.3	~ 2.3	375	0.216
$C_T = 2.5$	~ 0.1	~ 2.6	450	0.233
$C_T = 3.0$	~ 0.0	~ 3.0	500	0.256

In general, the maximum ballistic coefficient to reach subsonic conditions above 3 km altitude increases with thrust coefficient. Figure 8 showed the trend of total axial force coefficient for increasing thrust coefficient, with maximum benefit from aero-propulsive interactions near $C_T = 1.0$ and almost no aerodynamic drag contribution above $C_T \approx 3.0$. This is consistent with the approximate β limits given in Table 6. Increasing C_T increases the thrust magnitude, resulting in an increase in the total axial force coefficient. However, the difference between C_T and $C_{A,total}$ (the aerodynamic benefit) decreases with increasing C_T.

4. Comparison against Prior Studies – Constant Thrust Magnitude

Figure 19 shows the relationship between ballistic coefficient, initiation conditions, and final altitude. Design points from the study by Christian, et. al.[12] have been included for comparison, indicated by ∗ in Figure 19. Consistent with the prior study by Christian, et. al.[12], a constant thrust magnitude of 1 MN and a 15 m diameter Apollo aeroshell were assumed for all cases. As opposed to a constant thrust coefficient trajectory assumed previously, in these cases, the vehicle follows a constant thrust trajectory to a zero-velocity terminal condition. All data includes aero-propulsive interaction effects. The thrust coefficient values in Figure 19 are the C_T values at retropropulsion initiation. C_T varies with dynamic pressure over the trajectory. The design points from Christian, et. al.[12] are from pure lift-up trajectories; different hypersonic trajectories utilizing bank angle modulation to deliver the vehicle to conditions maximizing dynamic pressure for retropropulsion initiation will have lower thrust coefficients for higher mass systems. Figure 19 shows 0+ km final altitudes from favorable (limited C_D preservation) initial thrust coefficients for ballistic coefficients up to 400 kg/m^2. For the 15 m diameter aeroshell assumed for the cases in Figure 19, this corresponds to an entry mass of 91.9 t. For entry masses below ~ 100 t, the aerodynamic-propulsive interactions from supersonic retropropulsion can be significant, increasingly so for initiation conditions at higher dynamic pressures. This is also true for cases not following constant thrust trajectories.
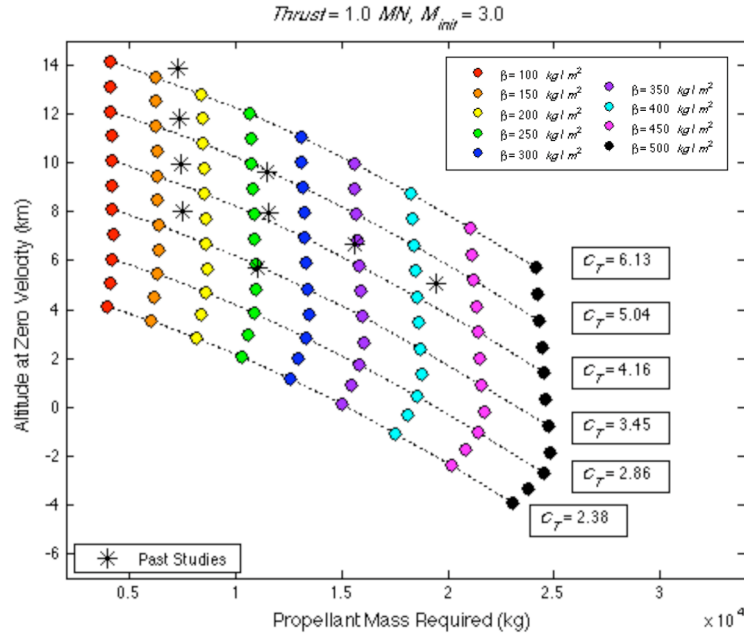
Figure 19. Propellant Mass Required for Constant Thrust Deceleration from Mach 3.0 to Zero Velocity

As expected, higher initiation altitudes correspond to higher altitudes of the final, zero velocity state. For common initiation conditions (altitude and Mach number), the final altitude decreases with increasing ballistic coefficient, consistent with results for constant thrust and a higher required ΔV. The data points for a specific ballistic coefficient correspond to initiation altitudes ranging from 5 km to 15 km. The sections of each ballistic coefficient contour at the lowest initiation altitudes bend away from the data points for higher initiation altitudes, indicating the ballistic coefficients and associated initiation conditions where aero-propulsive interactions are significant. This translates to initiation conditions corresponding to thrust coefficients less than 3.0. The point designs included in Figure 19 are for ballistic coefficients of 174, 261, 348, and 435 kg/m^2. Using the same initiation conditions as Christian, et. al.[12], Figure 19 shows these point designs to require initial thrust coefficients well above 3.0, or thrust coefficients for which there is essentially no aerodynamic force augmentation.

As was shown in Figures 15 and 16, the influence of the aero-propulsive interactions arising from initiating retropropulsion at supersonic conditions increases with ballistic coefficient and initiation Mach number. Figure 20 shows this same trend for retropropulsion initiation at Mach 3.0 for ballistic coefficients ranging from 100 to 500 kg/m^2. The difference between the propellant mass required when aero-propulsive effects are included and when these effects are neglected is only seen at thrust coefficients below 3.0, consistent with the model developed from experimental work by Jarvinen and Adams[15]. This difference grows with ballistic coefficient as a result of an increase in the required ΔV.
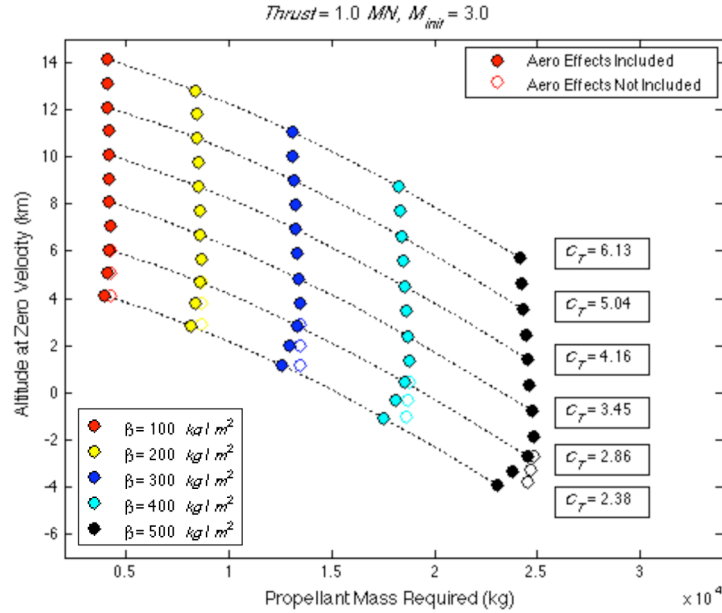
Figure 20. Increasing Significance of Aero-Propulsive Interactions with Ballistic Coefficient

VIII. Concluding Remarks

As vehicle masses continue to increase for missions involving atmospheric entry, supersonic deceleration is challenging the qualifications and capabilities of Viking-heritage EDL technology. At Mars, high entry masses and insufficient atmospheric density often result in unacceptable parachute deployment and operating conditions, requiring the exploration of alternative approaches to supersonic deceleration. Supersonic retropropulsion may be an enabling technology for systems with high ballistic coefficients operating in thin atmospheres such as at Mars. The relevance of this technology has been shown to increase with ballistic coefficient to the point that it is likely required for human Mars exploration.

For a fixed thrust coefficient, variation in supersonic descent propellant mass fraction was shown to be only a function of the required ΔV. The performance impact of aero-propulsive interactions (as measured by propellant mass fraction) is almost entirely dependent on thrust coefficient. Maximum reduction in required thrust coefficient to achieve the same axial deceleration force occurs near $C_T = 1.0$, and no reduction in required thrust coefficient occurs above $C_T \approx 3.0$.

For higher thrust coefficients, higher ballistic coefficient cases are possible (i.e., retropropulsion initiation below Mach 5.0 resulting in Mach 0.9 conditions above 3 km altitude) at the cost of a higher propellant mass fraction. At thrust coefficients corresponding to maximum aerodynamic augmentation performance benefit ($C_T \sim 1.0$), the ballistic coefficient limit was found to be ~ 350 kg/m^2 (~ 80400 kg entry mass for a 15 m diameter vehicle). Comparison of constant thrust cases with past studies found the point designs in prior studies utilized thrust coefficients greater than 3.0 (settings for which essentially no aerodynamic augmentation is possible). Hence, the assumption made in these studies of no aerodynamic performance benefit during supersonic descent has been shown to be generally valid. This study also demonstrated that initiating supersonic retropropulsion as late in the trajectory as possible (at lower altitudes) is advantageous as a result of both the lower ΔV requirements and the increased atmospheric density.

Thrust coefficients yielding significant aero-propulsive interaction performance benefits are achievable for ballistic coefficients up to ~ 450 kg/m^2 (Mach 3.0 initiation and 0+ km terminal altitude). The results of this preliminary assessment of the systems level performance of supersonic retropropulsion not only show supersonic retropropulsion to be a potentially enabling technology for advanced Mars exploration, but a technology extensible to high mass entry systems at potentially lower mass costs than predicted in prior Mars architecture studies.

References

[1] R.D. Braun and R.M. Manning, "Mars Exploration Entry, Descent, and Landing Challenges," <u>Journal of Spacecraft and Rockets</u>, Vol. 44, No. 2, 310-323, March – April 2007.

[2] E. Love, "The Effect of a Small Jet of Air Exhausting from the Nose of a Body of Revolution in Supersonic Flow," NACA RM L52I19a, November 1952.

[3] E. Love, "A Re-examination of the use of Simple Concepts for Predicting the Shape and Location of Detached Shock Waves," NACA TN-4170, 1957.

[4] E. Love, et al., "Experimental and Theoretical Studies of Axisymmetric Free Jets," NASA TR R-6, 1959.

[5] R. Huff and K. Abdalla, "Mixing Characteristics Downstream of Core Region of High-Temperature Axisymmetric Jets Exhausting into Transonic and Supersonic Streams," NASA TM X-151, March 1960.

[6] W. Moeckel, "Flow Separation Ahead of Blunt Bodies at Supersonic Speeds," NACA TN 2418, July 1951.

[7] W. Moeckel, "Flow Separation Ahead of a Blunt Axially Symmetric Body at Mach Numbers 1.76 to 2.10," NACA RM E51I25, December 1951.

[8] E. Love, M. Woodling, L. Lee, "Boundaries of Supersonic Axisymmetric Free Jets," NACA RM L56G18, October 1956.

[9] E. Love and C. Grigsby, "Some Studies of Axisymmetric Free Jets Exhausting From Sonic and Supersonic Nozzles into Still Air and Into Supersonic Freestreams," NACA RM L54L31, May 1955.

[10] B.G. Drake," Reference Mission Version 3.0: Addendum to the Human Exploration of Mars: The Reference Mission of the NASA Mars Exploration Study Team," NASA/SP-6107-ADD, June 1998.

[11] S.J. Hoffman (ed.) and D.I. Kaplan (ed.), "Human Exploration of Mars: The Reference Mission of the NASA Mars Exploration Study Team," NASA Johnson Space Center, July 1997.

[12] J. Christian, G. Wells, J. Lafleur, A. Verges, R. Braun, "Extension of Traditional Entry, Descent, and Landing Technologies for Human Mars Exploration," <u>Journal of Spacecraft and Rockets</u>, Vol. TBD, 2008.

[13] G. Wells, et al., "Entry, Descent, and Landing Challenges of Human Mars Exploration," *29th AAS Guidance and Control Conference*, AAS 06-072, Breckenridge, Colorado, February 2006.

[14] L.G. Tanner, "Development and Characteristics of the Russian / American RD-180 Rocket Engine," *AIAA Joint Propulsion Conference*, Liquid Propulsion Short Course, Indianapolis, Indiana, July 2002.

[15] P. Jarvinen and R. Adams, "The Aerodynamic Characteristics of Large Angled Cones with Retrorockets," NASA Contract No. NAS 7-576, February 1970.

[16] P.A. Gnoffo, "Planetary-Entry Gas Dynamics," <u>Annual Review of Fluid Mechanics</u>, Vol. 31, 459-494, 1999.

[17] J. Campbell, "Supersonic Aerodynamic Characteristics and Shock Standoff Distances for Large-Angle Cones with and without Cylindrical Afterbodies," NASA TN D-5334, 1969.

[18] P.J. Finley, "The Flow of a Jet from a Body Opposing a Supersonic Free Stream," <u>Journal of Fluid Mechanics</u>, Vol. 26, No. 2, 337-368, October 1966.

[19] E.A. Barber, "An Experimental Investigation of Stagnation-Point Injection," <u>Journal of Spacecraft and Rockets</u>, Vol. 2., No. 5, 770-774, May 1965.

[20] D. Romeo and J. Sterrett, "Exploratory Investigation of the Effect of a Forward-Facing Jet on the Bow Shock of a Blunt Body in a Mach Number 6 Free Stream," NAS TN D-1605, February 1963.

[21] E.O. Daso, V.E. Pritchett, and T.S. Wang, "The Dynamics of Shock Dispersion and Interactions in Supersonic Freestreams with Counterflowing Jets," *45th AIAA Aerospace Sciences Meeting*, AIAA 2007-1423, Reno, Nevada, January 2007.

[22] Watt, "An Experimental Investigation of a Sonic Jet Directed Upstream Against a Uniform Supersonic Flow," Institute of Aerophysics, University of Toronto TN 7, January 1956.

[23] R. McGhee, "Effects of a Retronozzle Located at the Apex of a 140° Blunt Cone at Mach Numbers of 3.00, 4.50, and 6.00," NASA TN D-6002, January 1971.

[24] V. Peterson and R. McKenzie, "Effects of Simulated Retrorockets on the Aerodynamic Characteristics of a Body of Revolution at Mach Numbers from 0.25 to 1.90," NASA TN D-1300, May 1962.

[25] P. Jarvinen and R. Adams, "The Effects of Retrorockets on the Aerodynamic Characteristics of Conical Aeroshell Planetary Entry Vehicles," AIAA 70-219, *AIAA 8th Aerospace Sciences Meeting*, New York, New York, January 1970.

[26] J.W. Keyes and J.N. Hefner, "Effect of Forward Facing Jets on Aerodynamic Characteristics of Blunt Configurations at Mach 6," Journal of Spacecraft and Rockets, Vol. 4, No. 4, 533-534, April 1967.

[27] N. Charczenko and K. Hennessey, "Investigation of a Retrorocket Exhausting from the Nose of a Blunt Body into a Supersonic Free Stream," NASA TN D-751, September 1961.

[28] D. Romeo and J. Sterrett, "Flow Field for Sonic Jet Exhausting Counter to a Hypersonic Freestream," AIAA Journal, Vol. 3, No. 3, 344-346, March 1965.

[29] R. Margason, "The Path of a Jet Directed at Large Angles to a Subsonic Free Stream," NASA TN D-4919, November 1968.

[30] A.F. Charwat and J. Allegre, "Interaction of a Supersonic Stream and a Transverse Supersonic Jet," AIAA Journal, Vol. 2, No. 11, 1965-1972, November 1964.

[31] P. Jarvinen and J. Hill, "Penetration of Retrorocket Exhausts into Subsonic Counterflows," Journal of Spacecraft and Rockets, Vol. 10, No. 1, 85-85, January 1973.

[32] L. Hayman and R. McDearmon, "Jet Effects on Cylindrical Afterbodies Housing Sonic and Supersonic Nozzles which Exhaust against a Supersonic Stream at Angles from 90 to 180 Degrees," NASA TN D-1016, March 1962.

[33] J. Baron and E. Alzner, "An Experimental Investigation of a Two Layer Inviscid Shock Cap due to Blunt Body Nose Injection," Journal of Fluid Mechanics, Vol. 15, No. 3, 442-448, March 1963.

[34] E.A. Barber, "An Experimental Investigation of Stagnation-Point Injection," *AIAA Conference on Physics of Entry into Planetary Atmospheres*, AIAA 1963-0433, Cambridge, Massachusetts, August 1963.

[35] C. Warren, "An Experimental Investigation of the Effect of Ejecting a Coolant Gas at the Nose of a Bluff Body," Journal of Fluid Mechanics, Vol. 2, No. 8, 400-417, 1960.

[36] L. Roberts, "Mass Transfer Cooling Near the Stagnation Point," NASA TR R-8, 1959.

[37] K. Hayashi, S. Aso, Y. Tani, "Numerical Study of Thermal Protection System by Opposing Jet," *43rd AIAA Aerospace Sciences Meeting*, AIAA 2005-0188, Reno, Nevada, January 2005.

[38] K. Hayashi and S. Aso, "Effect of Pressure Ratio on Aerodynamic Heating Reduction due to Opposing Jet," *33rd AIAA Fluid Dynamics Conference*, AIAA 2003-4041, Orlando, Florida, June 2003.

[39] J. Stalder and M. Inouye, "A Method of Reducing Heat Transfer to Blunt Bodies by Air Injection," NACA RM A56B27a, May 1956.

[40] J.E. Grimaud and L.C. McRee, "Experimental Data on Stagnation-Point Gas Injection Cooling on a Hemisphere-Cone in a Hypersonic Arc Tunnel," NASA TM X-983, July 1964.

[41] A.F. Grenich and W.C. Woods, "Flow Field Investigation of Atmospheric Braking for High Drag Vehicles with Forward Facing Jets," *AIAA 19th Aerospace Sciences Meeting*, AIAA 1981-0293, St. Louis, Missouri, January 1981.

[42] P. Chung, "Effect of Localized Mass Transfer Near the Stagnation Region of Blunt Bodies in Hypersonic Flight," NASA TN D-141, May 1960.

[43] M. Pindzola, "Jet Simulation in Ground Test Facilities," AGARDograph 79, November 1963.

[44] V.M. Fomin, A.A. Maslov, N.D. Malmuth, "Influence of a Counterflow Plasma Jet on Supersonic Blunt-Body Pressures," <u>AIAA Journal</u>, Vol. 40, No. 6, 1170-1177, June 2002.

[45] G.G. Chernyi, "Some Recent Results in Aerodynamic Applications of Flows with Localized Energy Addition," *9th International Space Planes and Hypersonic Systems and Technologies Conference*, AIAA 99-4819, Norfolk, Virginia, November 1999.

[46] A. Seiff, "Post-Viking Models for the Structure of the Summer Atmosphere of Mars," <u>Adv. Space Res.</u>, Vol. 2, 3-17, 1982.

[47] E.J. Christensen, <u>Journal of Geophysics</u>, Res., Vol. 80, 2909, 1975.

[48] N.X. Vinh, A. Busemann, and R.D. Culp, <u>Hypersonic and Planetary Entry Flight Mechanics</u>, University of Michigan Press: Ann Arbor, Michigan, 1980.